Available online at www.sciencedirect.com
ScienceDirect
Particuology 6 (2008) 347–361
PARTICUOLOGY
www.elsevier.com/locate/partic

Micromechanics of breakage in sharp-edge particles using combined DEM and FEM

Ahad Bagherzadeh-Khalkhali *, Ali Asghar Mirghasemi, Soheil Mohammadi

School of Civil Engineering, University College of Engineering, University of Tehran, P.O. Box 11155-4563, Tehran, Iran

Received 15 March 2008; accepted 2 July 2008

Abstract

By combining DEM (Discrete Element Method) and FEM (Finite Element Method), a model is established to simulate the breakage of two-dimensional sharp-edge particles, in which the simulated particles are assumed to have no cracks. Particles can, however, crush during different stages of the numerical analysis, if stress-based breakage criteria are fulfilled inside the particles. With this model, it is possible to study the influence of particle breakage on macro- and micro-mechanical behavior of simulated angular materials. Two series of tests, with and without breakable particles, are simulated under different confining pressures based on conditions of biaxial tests. The results, presented in terms of micromechanical behavior for different confining pressures, are compared with macroparameters. The influence of particle breakage on microstructure of sharp-edge materials is discussed and the related confining pressure effects are investigated. Breakage of particles in rockfill materials are shown to reduce the anisotropy coefficients of the samples and therefore their strength and dilation behaviors.

Keywords: DEM; FEM; Particle breakage; Rockfill; Micromechanics; Anisotropy; Confining pressure

1. Introduction

Behavior of granular media is related to mineralogical composition, particle grading, size, shape, fragmentation and stress conditions. Breakage of the constituent components (grains) of a soil structure due to imposed stresses, called "particle breakage", has arisen in many soil-rockfill masses such as rockfill dams and breakwaters as well as in many conventional laboratory tests under normal pressures.

The related phenomenon has been studied in various laboratory tests, e.g., triaxial, consolidation and uniaxial (Lade & Yamamuro, 1996; Lade, Yamamuro, & Bopp, 1996; Marsal, 1967, 1973), which showed that many engineering characteristics of granular materials such as strength (stress–strain behavior), deformability, pore pressure distribution and permeability are greatly influenced by the level of breakage of materials (Lade & Yamamuro, 1996; Lade et al., 1996). Marsal (1967), perhaps the first to deal with the concept of crushing of particles, verified the breakage phenomena of particles in rockfill materials in a large-scale triaxal test, summarizing his study as follows:

> "It seems that phenomenon of fragmentation is an important factor that impacts shear resistance and potentiality of compaction of grain materials and this phenomenon is effective on aforesaid parameters in different conditions of implementing stresses such as confining pressure stage or stage of divertive loading in triaxial test."

Among other researchers (Lade & Yamamuro, 1996; Yamamuro & Lade, 1996; Indraratna, Wijewardena, & Balasubramaniam, 1993), Varadarajan, Sharma, Venkatachalam, and Gupta (2003) presented the ratio of principal stresses (σ_1/σ_3) imposed on different rock materials at failure in triaxial tests. Also, many researchers demonstrated that particle breakage led to a reduction in void ratio, leading to compaction of the material. Marsal (1967) believed that changes in void ratio were due to new arrangement of particles after breakage. Lade and Yamamuro (1996) and Yamamuro and Lade (1996) concluded from testing sand under different confining pressures (from 0.5 to 70 MPa) that breakage of particles played the major role in changing the volume of the material.

* Corresponding author. Tel.: +98 21 8478 2066; fax: +98 21 8877 6648.
E-mail address: a_bagher_kh@Yahoo.com (A. Bagherzadeh-Khalkhali).

1674-2001/$ – see inside back cover © 2008 Chinese Society of Particuology and Institute of Process Engineering, Chinese Academy of Sciences. Published by Elsevier B.V.All rights reserved.
doi:10.1016/j.partic.2008.07.002

Nomenclature

a	anisotropy coefficient of contact normal
a_b	Hoek and Brown's constant coefficient, constant
a_n	anisotropy coefficient of normal force
a_t	anisotropy coefficient of tangential force
A	area of the assembly (m^2)
b	y-intercept of the failure line (m)
$E(\theta)$	portion of the total number of contacts that are oriented at angle θ
f_i^C	contact force between two discrete particles (N)
$\bar{f}_n(\theta)$	average normal contact force tensor (N)
$\bar{f}_t(\theta)$	average tangential contact force tensor (N)
$\bar{f}_n^0$	average normal contact force from all assembly contacts (N)
F_n	normal contact force (N)
F_s	shear contact force (N)
l_j^C	contact vector between two discrete particles
m	slope of the failure line
m_b	Hoek and Brown's constant coefficient, constant
M	total number of contact points within an assembly
N	total number of particles in an assembly
P_{cp}	confining pressure (MPa)
Rat	plastic indicator of the whole particle (%)
$RatF$	critical value of Rat (%)
S	Hoek and Brown's constant coefficient, constant
SF_i	safety factor of point i with the coordinates of (x_i,y_i)
SUM	total sum of error squares (m^2)
W_i	weighing coefficient of point i with the coordinates of (x_i,y_i)

Greek symbols

γ	average coordination number of an assembly
Δ_i	residual, y-error of point I (m)
ε_a	axial strain (%)
θ_0	major principal direction of anisotropy (rad)
θ_f	major principal direction of normal force anisotropy (rad)
θ_{fa}	angle of failure line against the major principal stress direction (rad)
θ_t	major principal direction of tangential force anisotropy (rad)
σ_c	uniaxial compression strength (MPa)
σ_{ij}	stress tensor (MPa)
σ_t	tensile strength (MPa)
$\sigma_1, \sigma_2, \sigma_3$	principal stresses (MPa)
σ_{1f}	major principal stress at failure (MPa)
ϕ	mobilized angle of friction (rad)

2. Particle breakage simulation

Cundall, a pioneer of using DEM (Discrete Element Method) in studying the behavior of granular media and stability of rock slopes, developed the RBMC code in which the breakage of rock blocks was simulated after the Brazilian test (Cundall & Hart, 1985). In each simulation cycle all point loads applied to each block are first checked and then the points of application and magnitudes of two maximum loads, applied in opposite directions, are determined. Potapov and Campbell (1994, 1997) studied the breakage of a single spherical particle that impacts on a solid plate and the brittle particle attrition in a shear cell.

Simultaneous use of DEM and MD (Molecular Dynamic) has recently been applied to breakage modeling and crack formation in brittle bodies. MD considers a macroscopic material as an assemblage of microscopic particles. Kun and Herrmann (1996) considered each block as a mesh of inter-connected tiny cells located in a plane, each rigid convex polygon of which acts as the smallest component of the block.

To study the influence of particle breakage on macro- and micro-mechanical parameters for two-dimensional polygon-shaped particles, Seyedi Hosseininia and Mirghasemi (2006, 2007) presented a DEM model, in which each uncracked particle (convex polygon) is replaced by a group of smaller inter-connected bonded rigid sub-particles. If the bond between the sub-particles breaks, breakage will occur.

Robertson and Bolton (2001) and McDowell and Harireche (2002) simulated three-dimensional crushable soils by using DEM, implemented as the PFC^{3D} computer code (Itasca Consulting Group, 1999) in which agglomerates are constructed by bonding elementary spheres in 'crystallographic' arrays. Both stiffness bonding and slip models are included in their constitutive representation of contact points between the elementary spheres. Bond strength limits are enforced for the total normal and shear contact forces. The bond breaks if either of these limits is violated.

A slip model applies between unbonded objects in contact, or between bonded objects when their contact breaks, to limit the shear force between the objects in contact and to allow slip to occur at some limiting shear force, governed by Coulomb's law. This approach has been used for simulating silica sand grains and the results compared favorably with available real data (Cheng, Nakata, & Bolton, 2003), though it can not be used for particles with sharp angles such as rockfills.

3. Particle breakage modeling in this research

In this research, particle breakage for rockfill (sharp-edge) materials is simulated by a new methodology. The main object is the discrete element simulation of particle breakage in rockfill materials during biaxial test, that is, a 2-d shear test in which a vertical deviatoric strain is applied under a constant horizontal confining stress. In most simulations of particle breakage, a particle is assumed to be inter-connected by bonding with sub-particles. If the bond between the sub-particles breaks, breakage will happen. In this research by using combined DEM and FEM, the breakage path is assumed to be a straight line, determined according to a full finite element stress-strain analysis of each particle, though successful application of the combined discrete and finite element methods has already been reported (Mohammadi, Owen, & Peric, 1998; Ghabousi, 1997).

In our proposed method, all particles are simulated as an assembly of discrete elements. At each step of DEM analysis, each particle is modeled by FEM to check for possible breakage. The breakage analysis of each particle will be performed based on its loading and present stress conditions. When a particle breaks, two new particles are generated, replacing the original one. This procedure is carried out on all particles for each time step of the discrete element model. The procedure begins by adopting the POLY software (Mirghasemi, Rothenburg, & Matyas, 1997, 2002) for modeling assemblies of irregularly sharp-edge shaped particles. In the second stage, a newly developed FEA (Finite Element Code) is used to check for breakage of particles.

3.1. Determination of breakage line

In an assembly of particles, each particle is considered intact without any joints and cracks. Particles at each DEM time step are analyzed separately using FEM according to the imposed loads from neighbouring particles. The resulting distribution of stresses in a particle allows for determination of plastic elements in the particle with the help of the Hoek–Brown failure criterion (Hoek & Brown, 1980, 1997). The probability of breakage in a particle and the potential breakage line are estimated based on the plastic elements.

In consideration of the geometrical shape of particles, the triangular linear element (3-node) was chosen for FEM analyses. A particle's boundary conditions, determined on the basis of its contact points with adjacent particles, are defined as the loading and the fixed points on the boundary. Two of the contact points are assumed as fixed points while the remaining contact points are considered points of external loading. The quantity of load is determined from the DEM contact force between particles. The stress–strain analysis of a linear polygon-shaped area is considered for static conditions, and the assumption of linear elastic behavior is accepted for intact rocks.

In order to control the process of breakage of particles, different criteria based on the plastic elements within the finite elements of a particle have been adopted. Different constitutive models such as Mohr–Coulomb, Hoek–Brown, Griffith, Morel, Franklin, Hobs, etc. could be used as a basis for determining instant of rock failure, among which, the Hoek–Brown failure criterion has been selected to determine the state of plastic conditions in rock (Hoek & Brown, 1980):

$$\begin{aligned} &\sigma_{1\mathrm{f}} = \sigma_3 + \sigma_\mathrm{c}((m_\mathrm{b}\sigma_3)/\sigma_\mathrm{c} + 1)^{0.5}, \sigma_3 > -\sigma_\mathrm{c}/m_\mathrm{b} \\ &\sigma_{1f} = \sigma_3, \sigma_3 \le -\sigma_\mathrm{c}/m_\mathrm{b} \end{aligned} \tag{1}$$

In this criterion, the coefficient m_b is a constant based on characteristics of rock and σ_c is the uniaxial compression strength of rock.

Elements undergoing tensions larger than $-\sigma_\mathrm{c}/m_\mathrm{b}$, fail in tension, whereas failure in elements with a high compressive stress occurs when the major principal stress is equal to or larger than $\sigma_{1\mathrm{f}}$, obtained from criterion (1). Therefore, safety factors for an element against plastic failure can be defined as:

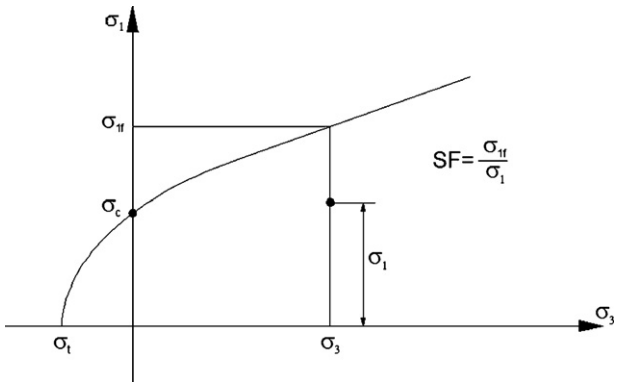

Fig. 1. Calculation of safety factor for shear elements.

$$\begin{aligned} &\mathrm{SF(tensile\ elements)} = \frac{\sigma_\mathrm{t}}{\sigma_3}, \\ &\mathrm{SF(shear\ elements)} = \frac{\sigma_{1\mathrm{f}}}{\sigma_1} \end{aligned} \tag{2}$$

The parameters in Eq. (2) are shown schematically in Fig. 1 for a shear element. Safety factors equal to or greater than 1 indicate intact elements, while smaller than 1, plastic failure occurs. Two methods are available for determining a linear path based on a set of pre-determined points, viz., based on least square of error for either horizontal distances (method X) or vertical distances (method Y) of points to the line. With these two methods all points equally affect the determination of the straight line. Numerically, elements with minimum safety factors are likely to be those that reach the first stage of plastic failure and further development of other plastic elements usually occurs around them. Therefore, definition of a weighting coefficient (W_i) is useful to enhance the accuracy of determining a breakage path. Such weighting coefficient of point i with the safety factor SF_i can be defined as:

$$W_i = \frac{1}{\mathrm{SF}_i} \tag{3}$$

Earlier plastic elements shall have greater weighting coefficients. As a result, they will have greater effect on the breakage line; i.e., the line will remain closer to these points. Weighting coefficients are implemented in both X and Y least square methods. If the least square method in Y direction is considered and the equation of the best line is assumed to be from n points with accurate coordinates (x_i,y_i) $(Y = mX + b)$, then the total sum of error squares is:

$$\begin{aligned} &\Delta_i = y_{i(\mathrm{accurate})} - y_{i(\mathrm{calculated})} \\ &y_{i(\mathrm{calculated})} = m x_{i(\mathrm{accurate})} + b \\ &\mathrm{SUM} = \sum_{i=1}^{n} W_i \Delta_i^2 \end{aligned} \tag{4}$$

Minimization of SUM with respect to m and b, $((\partial\mathrm{SUM}/\partial m) = 0)$ and $((\partial\mathrm{SUM}/\partial b) = 0)$, respectively, allows for evaluation of optimum values of m and b as follow. A similar approach can be adopted for the X-weighted least squares

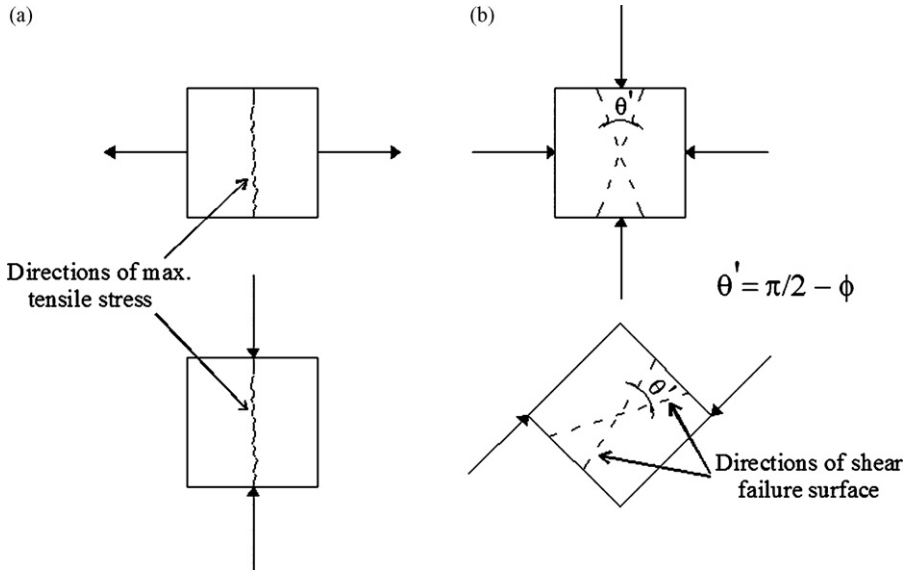

Fig. 2. Failure surfaces of tensile and shear modes: (a) tensile mode; (b) shear mode.

method.

$$m = \frac{\sum w_i \sum w_i x_i y_i - \sum w_i x_i \sum w_i y_i}{\sum w_i \sum w_i x_i^2 - (\sum w_i x_i)^2},$$

$$b = \frac{\sum w_i x_i^2 \sum w_i y_i - \sum w_i x_i \sum w_i x_i y_i}{\sum w_i \sum w_i x_i^2 - (\sum w_i x_i)^2} \quad (5)$$

As mentioned, two independent breakage lines are definable for each particle according to plastic elements. The first step towards selection of the final breakage line is to decide how to choose one of the above methods. Numerical studies have shown that the slope of failure surface in the first plastic element can be considered a proper criterion for selection of the final breakage line. Accordingly, the first crack is created in and propagated along the first plastic element. Thus, a breakage line close to the failure line for the first plastic element is selected as the final breakage line.

The main failure modes in rock are tensile and shear ruptures. In a rock element that reaches rupture under tension, the direction of maximum tension will be the failure line (Fig. 2(a)). If rock reaches shear failure, two different directions can be anticipated for breakage, which make a central angle of $((\pi/2) - \phi)$, as shown in Fig. 2(b). The angle for one of the failure directions against the major principal stress direction is:

$$\theta_{fa} = \frac{\pi}{4} + \frac{\phi}{2} \quad (6)$$

In 2002, Hoek defined the following relation between parameters of Hoek–Brown criterion and ϕ (Edelbro, 2004):

$$\phi = \sin^{-1}\left[\frac{6a_b m_b (S + m_b\sigma_3)^{a_b - 1}}{2(1 + a_b)(2 + a_b) + 6a_b m_b (S + m_b\sigma_3)^{a_b - 1}}\right] \quad (7)$$

In this equation, parameters a_b, m_b and S are Hoek–Brown parameters for the rock mass. $a_b = 0.5$ and $S = 1.0$ are used for an intact rock, and m_b can be defined from experimental triaxial tests or based on tables suggested by other researchers (Marinos & Hoek, 2001).

3.2. Proposed mechanism of breakage in a particle

An important step is the selection of a proper criterion for particle breakage and determination of geometrical specifications of newly generated particles. The plastic indicator of the whole particle (*Rat*) is suggested as criterion for determining the occurrence of crushing, which, for the whole particle, (*Rat*), is defined as the ratio of total number of plastic elements to the total number of elements of that particle. The selection of critical plastic indicator is based on laboratory data which include 51 unconfined tests of intact rocks from dam projects in Iran with different specifications such as diorite, basalt, quartz and limestone. These tests were simulated by FEM, by assuming the entire rock as homogeneous and isotropic and ignoring 3D effects. Fig. 3 shows an example of comparing unconfined experimental test with numerical simulation.

The values of *Rat* at the failure, i.e., *RatF* as the critical value, were determined for testing FEM simulations. Figs. 4 and 5 illustrate respectively the effect of Poisson's ratio and UCS (Unconfined Compression Strength) of rock on *RatF*. The relation between this critical value and the mechanical parameters of rock is apparently opposite, that is, as elastic modulus of rock increases, rock samples fail with low plastic indicators, indicating higher fragile behavior which causes crushing of such materials before developing major plastic zones. The same variation is also observed with increasing UCS. In general, the critical plastic indicator is proposed to be about 0.32–0.39 and the average value of *RatF* is 0.34. In this research, the critical value of plastic indicator at failure is assumed to be 0.4. It is recommended to conduct laboratory tests, such as the unconfined test, on rocks to determine values of critical plastic indicators.

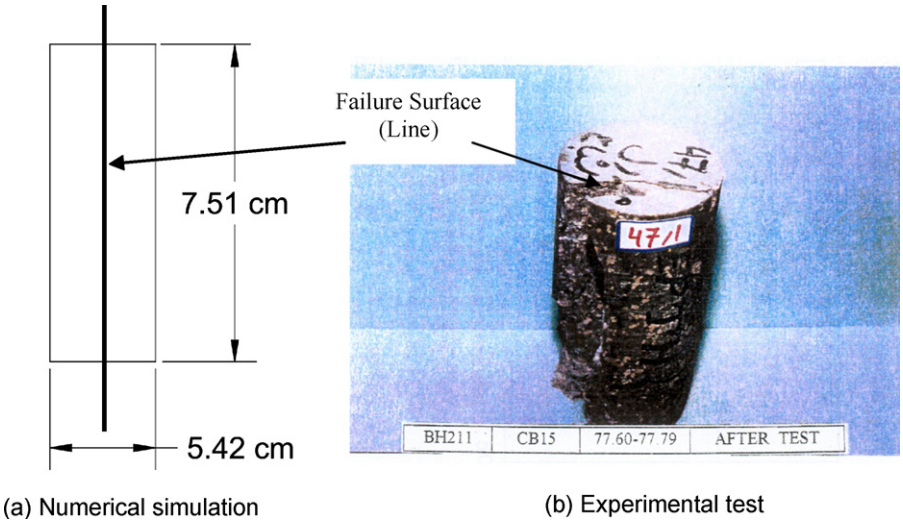

Fig. 3. Comparison of numerically predicted failure line and observed failure.

3.3. Simulations and parameters

To investigate the effect of particle breakage on micromechanics of sharp-edge materials, several biaxial tests with different confining pressures were simulated on assemblies of at least 500 particles each. Two series of tests were simulated for each confining pressure.

The biaxial tests are simulated in a drained condition for four successive stages including compaction of initially generated assembly of particles, relaxation of compacted assembly, application of hydrostatic pressure and finally shearing of the assembly. The initially generated assembly is loose and needs to be compacted before biaxial test. By applying strain control, boundary particles are moved towards the center of the assembly with a constant strain rate, as illustrated in Fig. 6 for the displacement trajectories of particles. The movement of boundary particles results in displacement of internal particles towards the assembly centre and therefore compaction of the assembly. A strain control at zero rate is applied to the assembly for relaxation. The boundary is fixed in place but the particles inside the assembly are allowed to receive minimal contact force.

A biaxial test starts by applying the confining pressure which is simulated as a stress control loading. The mobilized strain of particle is controlled in such manner that the average internal

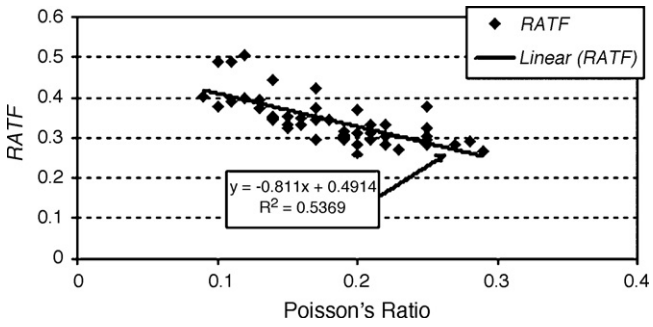

Fig. 4. Variations of plastic indicators versus Poisson's ratio in unconfined compression tests.

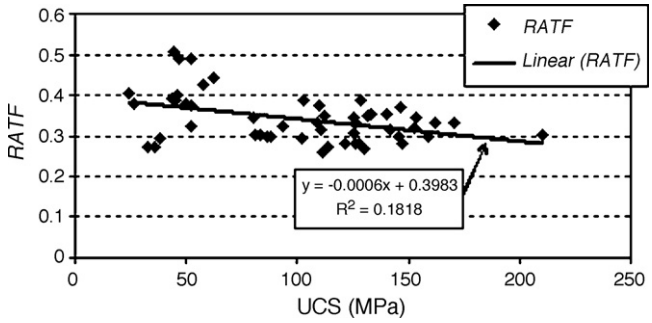

Fig. 5. Plastic indicators at failure versus rock unconfined compression strength in unconfined tests.

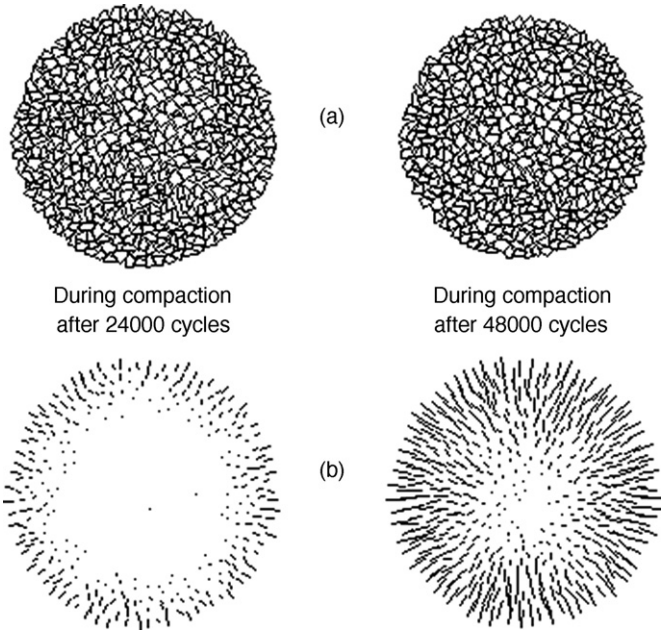

Fig. 6. Isotropically compacted assembly: (a) assembly of particles during compaction; (b) displacement trajectories of all particles during compaction.

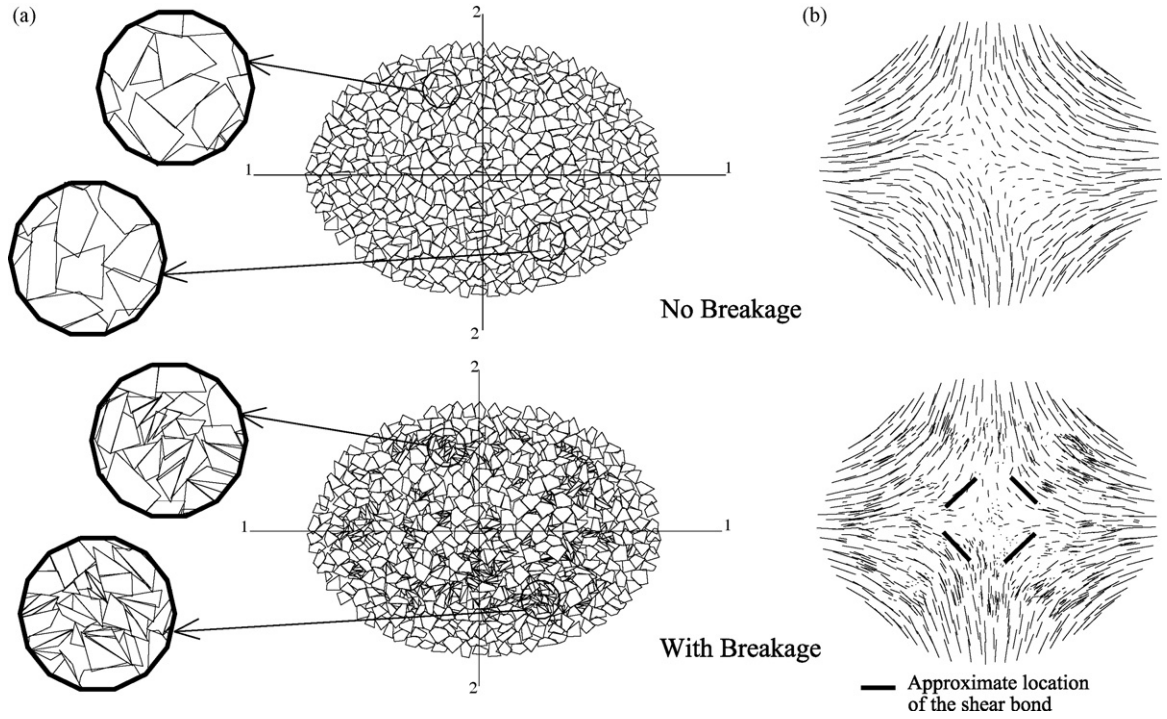

Fig. 7. Properties of particle assembly after shearing for confining pressure of 14.0 MPa: (a) assembly of particles at failure; (b) displacement trajectories of all particles after shearing.

stress of particles reaches the confining pressure. This confining loading will continue until a balance is achieved between the predefined external hydrostatic pressure and internal stresses. Fig. 7 shows the axial strain is applied in direction 2-2 with a constant confining pressure in direction 1-1 at the shearing stage. Simulation is continued until an axial strain of about 20% is reached. Fig. 7(a) shows the sheared assembly ($\varepsilon_a = 18\%$) under a confining pressure of 14 MPa, for both simulated test, with and without breakage, and Fig. 7(b) shows the displacement trajectories of particles during this stage including the shear bonds within the assembly as induced in four paths between axial and lateral directions.

In both test groups, no possibility for breakage (NB) and with possibility of breakage (WB), the friction coefficient between particles is set at 0.5 and contacts between particles are assumed cohesionless. Simulations are carried out under confining pressures of 0.5, 1, 2, 4, 8 and 14 MPa, and the 2D particles are assumed weightless. Table 1 shows the other parameters used in the simulations.

3.4. Review of the particle breakage process

Fig. 8 shows the mechanisms underlying the simulation of the breakage phenomenon for a WB test under a confining pressure of 0.5 MPa to illustrate the values of *Rat* computed from FEM analysis. In Fig. 8(a) the size of each solid point in this figure represents its value of *Rat*, for which the three sizes ($Rat \geq 0.4$) fulfill the breakage criteria for a particle. Fig. 8(b) shows that particles with *Rat* greater than the criteria are crushed.

Table 1
Parameters used in simulations

Normal and tangential stiffness (N/m)	2×10^7
Unit weight of particles (kg/m^3)	2500
Friction coefficient	0.5
Strain rate (%)	0.005
Modulus of elasticity (E) (MN/m^2)	7×10^4
Poisson's ratio (ν)	0.17
Rock strength parameters	
Compressive strength (MN/m^2)	300
m_b	25.0
S	1.0
a_b	0.5

Fig. 9 shows the transfer paths of normal contact forces (F_n) and shear contact force (F_s) among the particles, in particular, the two particles, numbered 48 and 377, with two contact locations assumed as fixed and other remaining contacts as externally loaded. The loads and fix points are shown to confirm the breakage path obtained by simulation.

4. Results and discussion

4.1. Microstructure of assembly

One way of investigating how a microstructure of granular assembly evolves during shear is to trace the displacement of each particle, as shown in Fig. 7 for the movement of all particles during both WB and NB tests at a confining pressure (P_{cp}) of 14.0 MPa. In this sketch, the initial and final locations of all

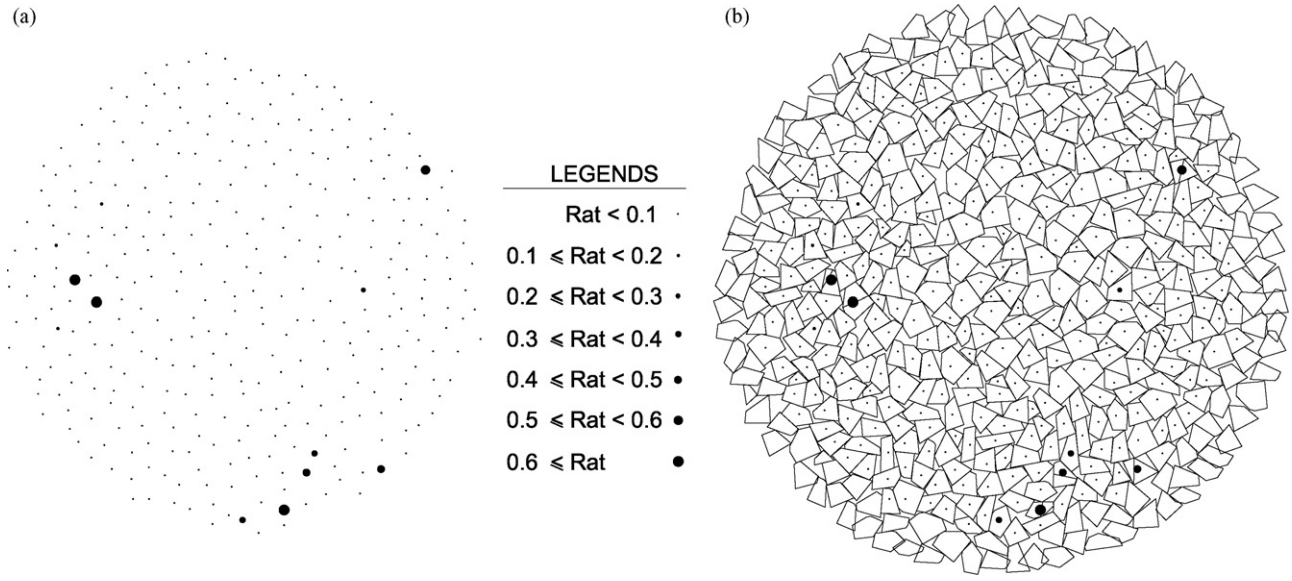

Fig. 8. Values of *Rat* parameter in simulated assembly at beginning of shearing in sample with confining pressure of 0.5 MPa.

particles are connected to each other, to show that the particles situated in the centre of the assembly have less movement. Fig. 10 shows the movement vectors of all particles at different stages of shearing under $P_{cp} = 2.0$ MPa. As a result, the shear bond location where the maximum differences between adjacent movement vectors are identified (Fig. 7), and by increasing the shearing strain, the shear bond moves towards the assembly centre.

Fig. 11 shows the transfer of normal contact forces between particles at a confining pressure of 2.0 MPa. Each normal contact force between two neighbouring particles is shown by a line and the thickness of lines demonstrates its magnitude. The induced

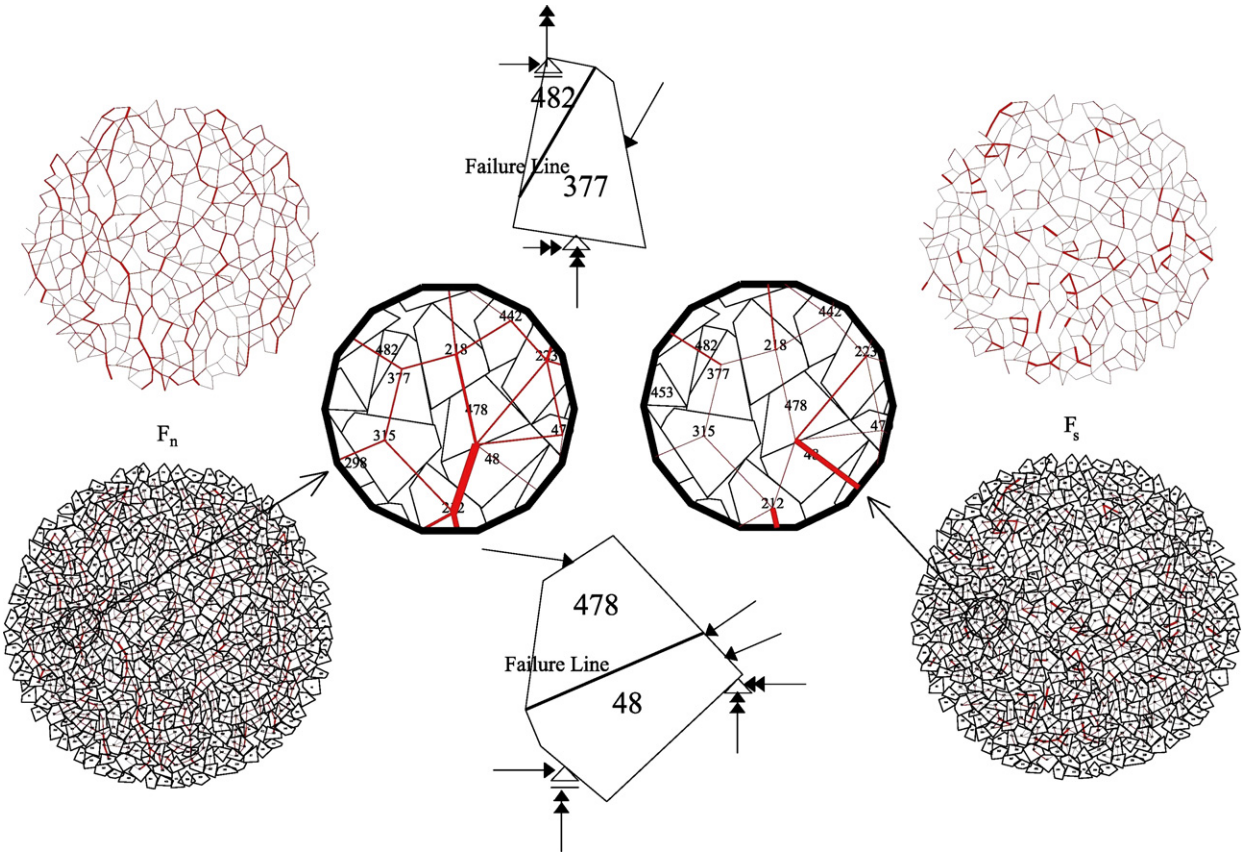

Fig. 9. Proposed simulation method of the particle breakage.

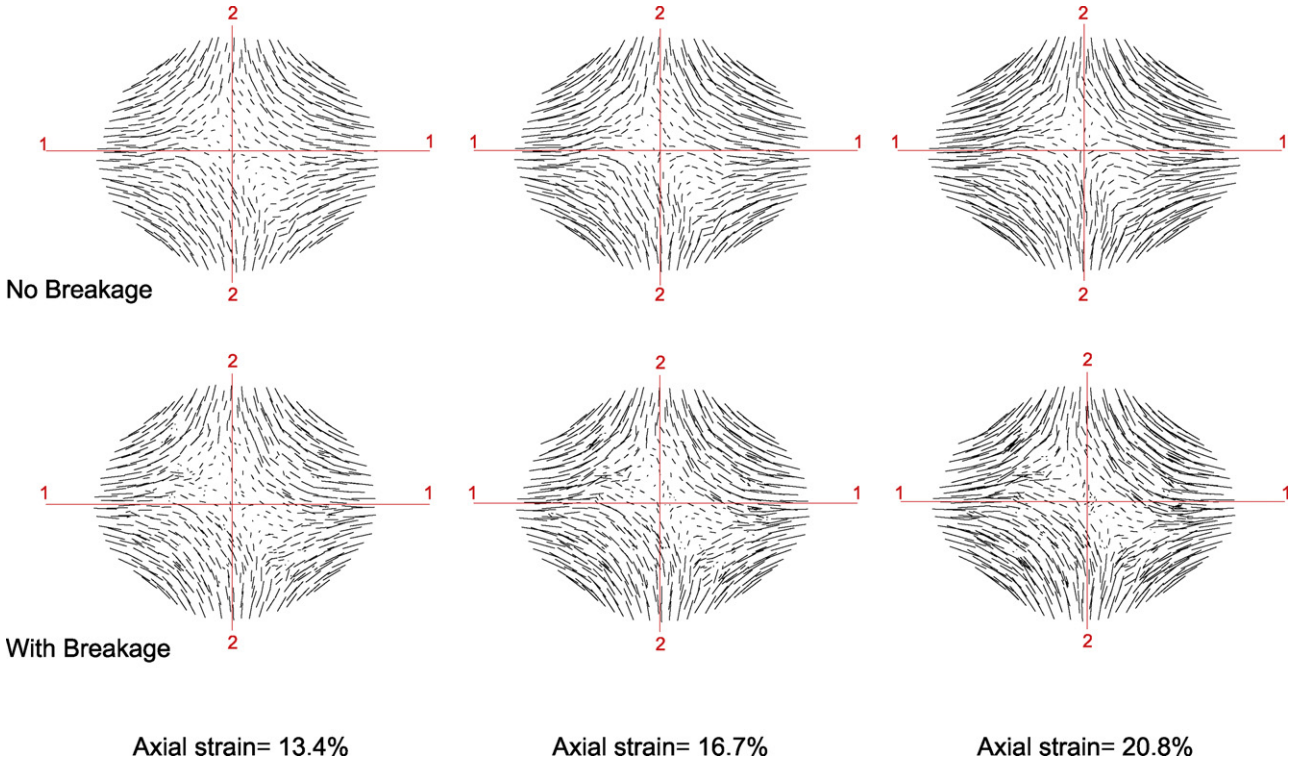

Fig. 10. Mobilized shear paths during biaxial NB and WB tests under a confining pressure of 2.0 MPa at different strain levels.

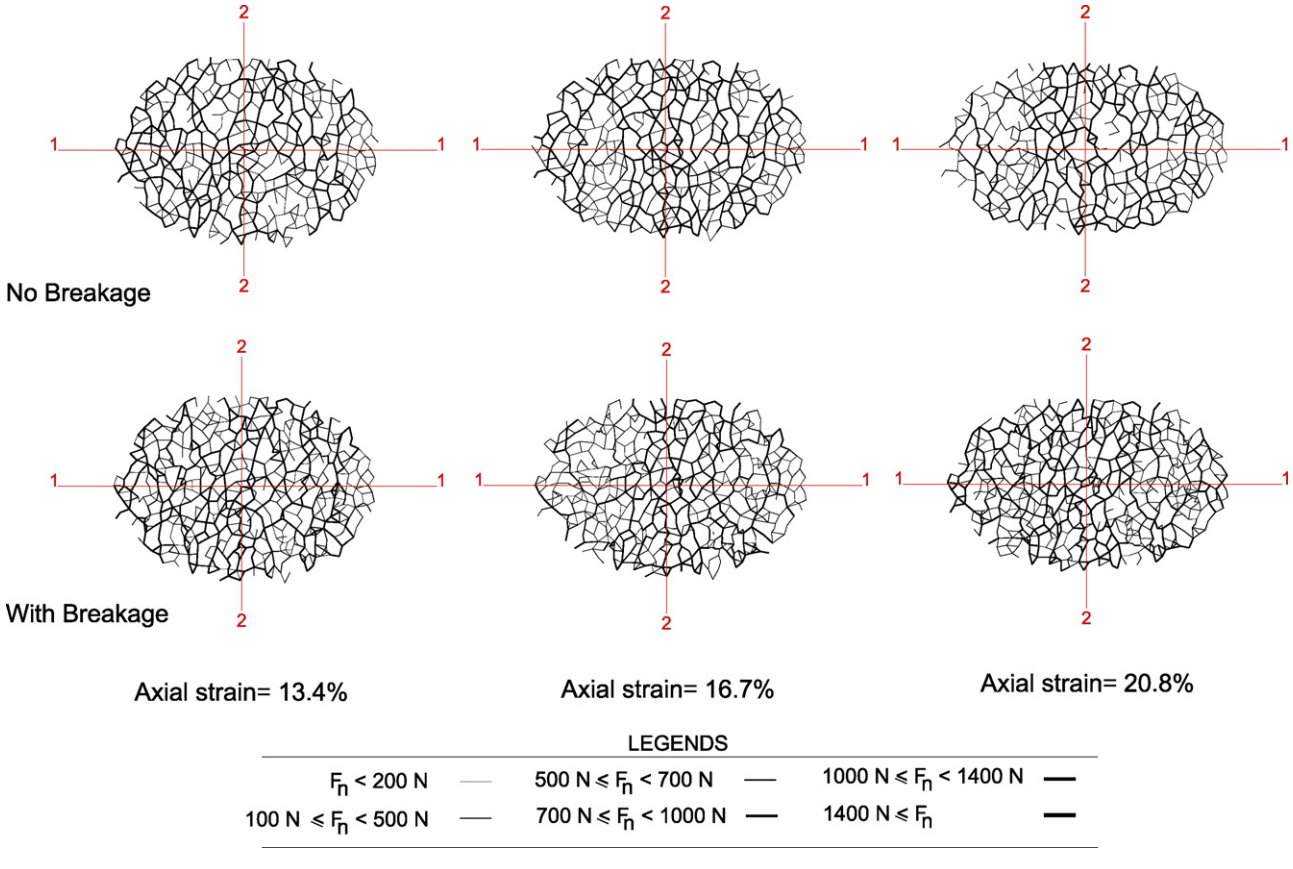

Fig. 11. Transfer paths of normal contact forces between particles during shearing under a confining pressure of 2.0 MPa at different strain levels.

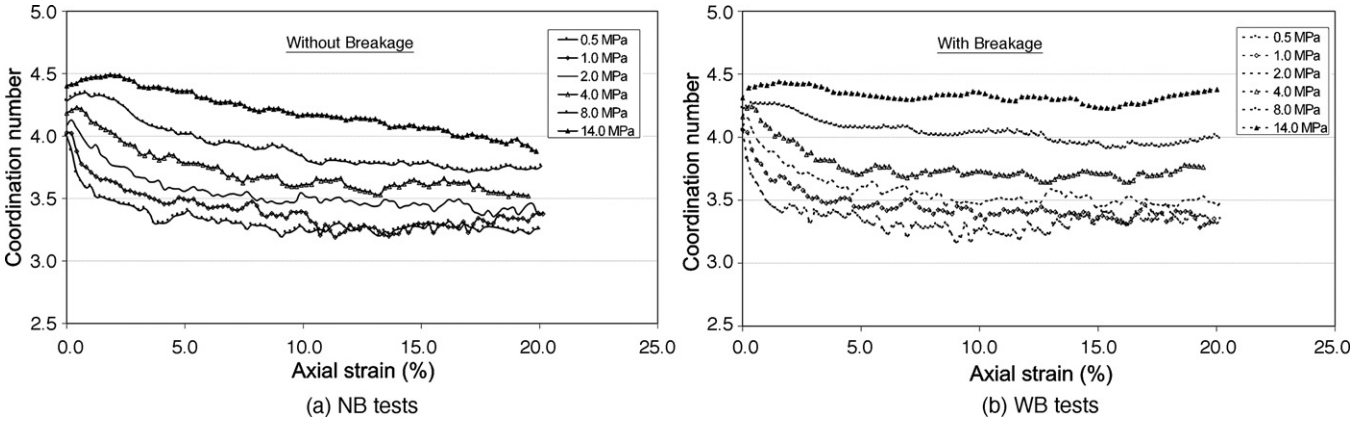

Fig. 12. Variation of coordination number with axial strain at different confining pressures: (a) NB tests; (b) WB tests.

contact normal forces in the vertical direction are greater than those in the horizontal direction since higher stresses are applied along the vertical direction.

4.2. Coordination number

Other way of investigating the evolution of microstructure of granular assembly is to study the change in the average number of contacts in the assembly or the average coordination number. The average coordination number, γ, of the assembly is:

$$\gamma = \frac{M}{N} \tag{8}$$

where M represents the total number of contact between particles within the assembly volume and N is the total number of particles.

Fig. 12 presents the evolution of the average coordination number during shear deformation at different confining pressures. The coordination number of the assemblies under both NB and WB tests decreases due to internal deformations and reaches some nearly constant value at large strain. Assemblies with breakable particles demonstrate less reduction in coordination number, because particles, upon breaking, create more particles which score more new contacts with their neighbours. Fig. 13 illustrates the variation of coordination number within an assembly for both NB and WB tests under a confining pressure of 2.0 MPa. Each solid point in the figure is defined as a particle and its diameter is related to the number of contacts between that particle and its neighbours. For both tests, contacts in the assembly begin to degrade as axial stress increases, mainly as a result of dilation in the horizontal direction. But for WB tests, particle breakage is also happening at the same time to result

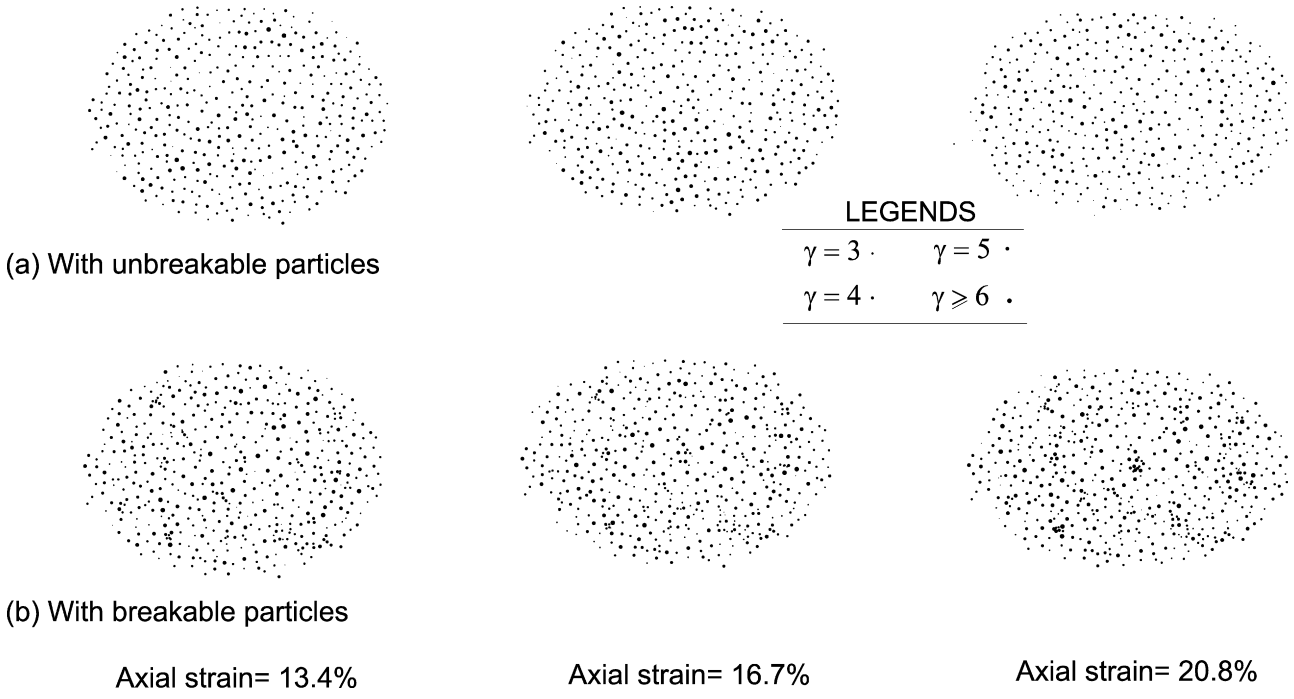

Fig. 13. Effect of the particle breakage on coordination number distribution in an assembly under a confining pressure of 2.0 MPa: (a) with unbreakable particles; (b) with breakable particles.

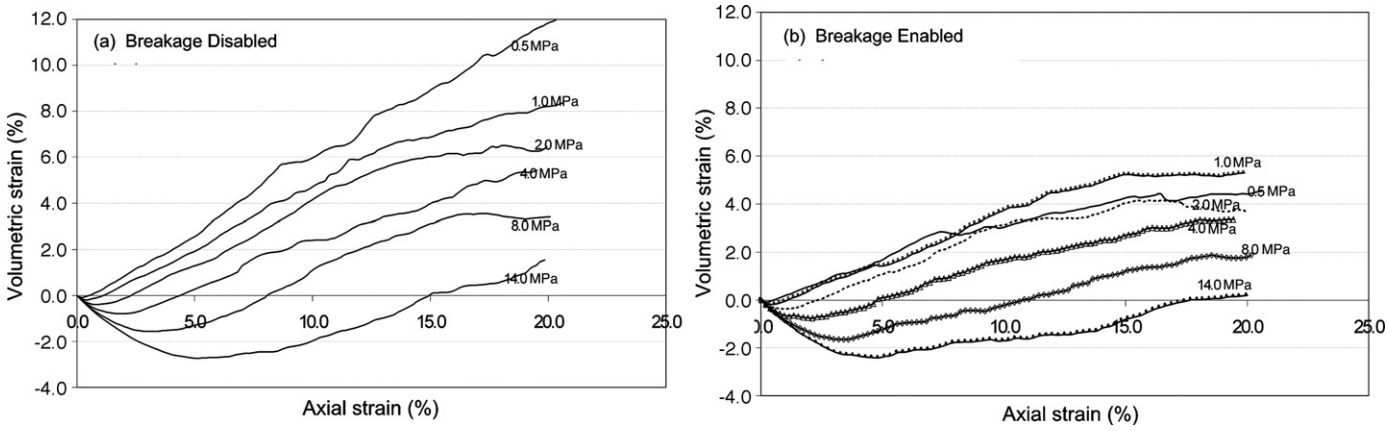

Fig. 14. Relationship between volumetric strain and axial strain at different confining pressures (from 0.5 to 14.0 MPa).

in more contacts between particles, thus increasing the coordination number. Fig. 12 shows the effect of confining pressure on coordination number: the higher the confining pressure, the more contacts are created in the assembly.

Fig. 14 shows the relationship between volumetric strain and axial strain under different confining pressures. Comparison between Fig. 14(a) and Fig. 14(b) shows that particle breakage decreases dilation and increases contraction. Less dilation decreases the possibility of contacts degeneration, therefore leading to greater coordination number, which is in agreement with Fig. 12.

4.3. Micromechanical coefficients of anisotropy

While forces in granular media must be carried by means of contacts between particles, a means of quantifying the

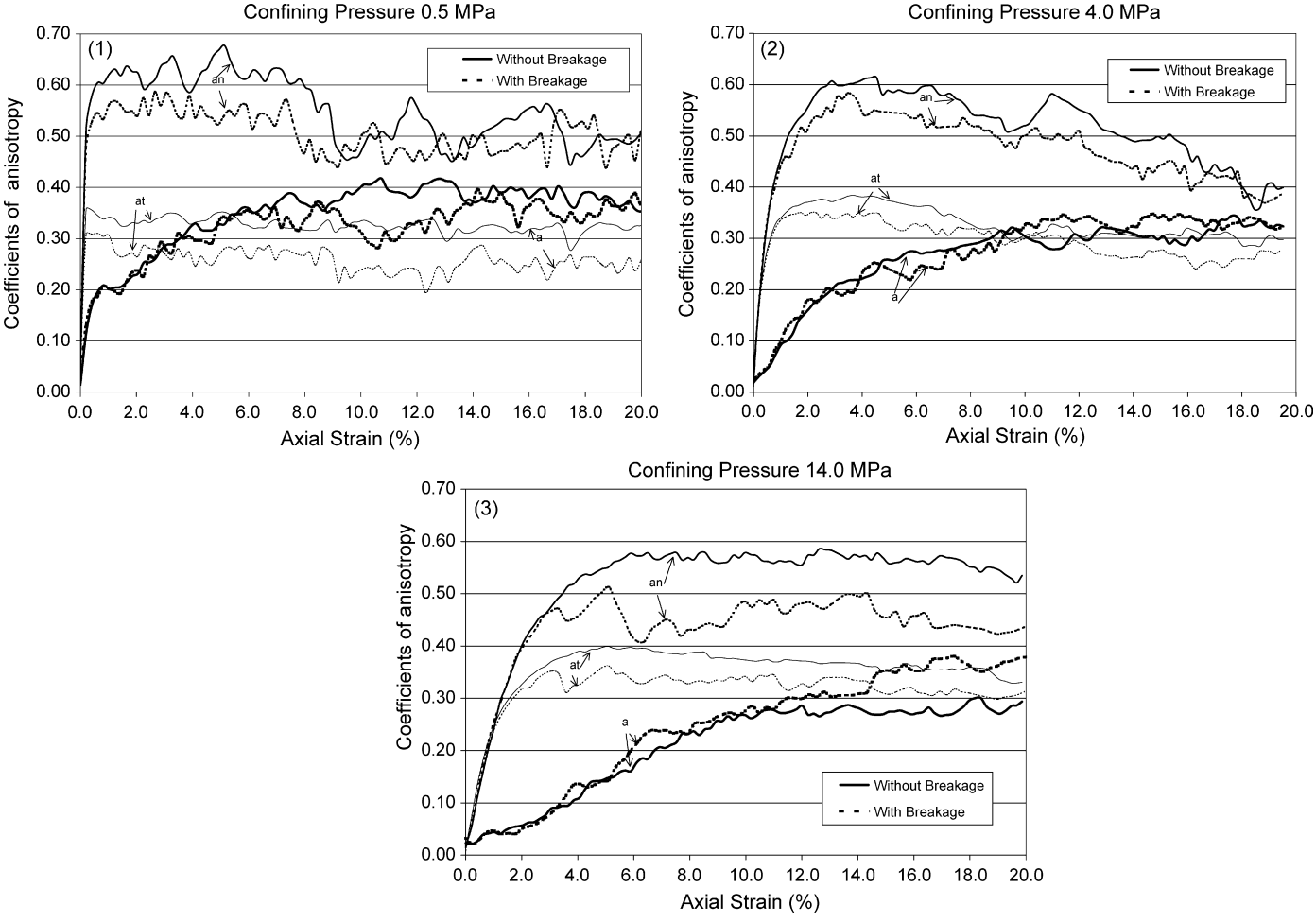

Fig. 15. Particle breakage effects on anisotropy coefficients at three stress levels (confining pressures of 0.5, 4.0 and 14.0 MPa).

arrangement of contacts has only recently been developed. For any angle θ, the portion of the total number of contacts in the system that are oriented at angle θ is $E(\theta)$. The distribution of normal contact orientations is described by a function such that the fraction of all assembly contact normal falls within the orientation interval $\Delta\theta$. Rothenburg et al. (1989) showed that the distribution of such contacts takes the form:

$$E(\theta) = \frac{1}{2\pi}\left[1 + a\ \cos 2(\theta - \theta_0)\right] \tag{9}$$

where a is referred to as the parameter of anisotropy, and θ_0 is the major principal direction of anisotropy. The meaning of a becomes clear if it is noted that the number of contacts oriented along the direction of anisotropy, i.e. when $\theta = \theta_0$, is proportional to $(1+a)$ while the number of contacts oriented in the perpendicular direction is proportional to $(1-a)$. The parameter a is therefore proportional to the difference in the number of contacts oriented along the direction of anisotropy and in the perpendicular direction. A similar expression was introduced by Thornton and Barnes (1986).

The magnitudes of the contact forces in an assembly vary from contact to contact. Despite the apparent randomness in the variation of contact forces, regular trends emerge when they are averaged over groups of contacts with similar orientations. The average contact force acting at contacts with an orientation can be decomposed into an average normal force component, $\bar{f}_n(\theta)$, and an average tangential force component, $\bar{f}_t(\theta)$. By averaging the contact forces of the contacts falling within the group of similar orientation and following the same logic as for the contact normal, symmetrical second-order tensors may be introduced to describe average normal contact forces and average tangential contact forces as follows (Rothenburg, Bathurst, & Dusseault, 1989):

$$\bar{f}_n(\theta) = \bar{f}_n^0\left[1 + a_n\ \cos 2(\theta - \theta_f)\right] \tag{10}$$

$$\bar{f}_t(\theta) = -\bar{f}_n^0\left[a_t\ \sin 2(\theta - \theta_t)\right] \tag{11}$$

where a_n is the coefficient of normal force anisotropy, and θ_f is the major principal direction of normal force anisotropy; $\bar{f}_n^0$ is the average normal contact force from all assembly contacts. Also, a_t and θ_t are the coefficients of tangential force anisotropy and the direction of anisotropy, respectively.

Fig. 15 shows the variations of anisotropy coefficients during shear deformation under three confining pressures. The coefficient of normal force anisotropy (a_n), which is higher than that in the tangential direction (a_t), generally evolves to some peak value and then reduces slowly to some lower ultimate values at large axial strains except for tests under high stress levels.

In both WB and NB tests, by applying a deviatoric axial strain in the vertical direction, the normal forces carried by chains of particles in the vertical direction are increased, while the magnitude of average normal forces in the horizontal direction remains almost constant. In test with a low confining pressure, as the axial strain increases, a_n shows a rapid growth at lower axial strain, followed by a reduction after some maximum value, apparently because of loss of contacts and loss of the capacity of chains of particles to sustain high forces. On the other hand, when the imposed confining pressure is higher, a_n shows a gradual increase which reaches some constant value. These trends are the same for both groups of assemblies involving rigid or breakable particles.

Fig. 15 also shows that the variation of tangential force anisotropy (a_t) grows rapidly to some peak value at the beginning of shearing but with increasing strain, it reduces slowly up to the end of the test. The initial increase in a_t is due to the development of frictional resistance as a result of potential relative movement between adjacent particles. As the number of contacts reduces, the particles gain more opportunity to rotate; therefore in NB test, tangential forces are slowly released. In WB tests, particles cannot bear any more tangential forces and break into pieces so they have more opportunity to move freely in the voids between other particles. For this reason, particle breakage restricts mobilization of the shear forces completely; and so anisotropy reduces.

Fig. 16 shows the effect of confining pressure on the evolution of anisotropy coefficient of contact normal (a) indicating that the confining pressure has a reverse effect on this coefficient, but this rule is not seen at large strain values for WB tests (Fig. 16(b)). It can be due to the role of new particles which are created as a result of breakage within the assemblies.

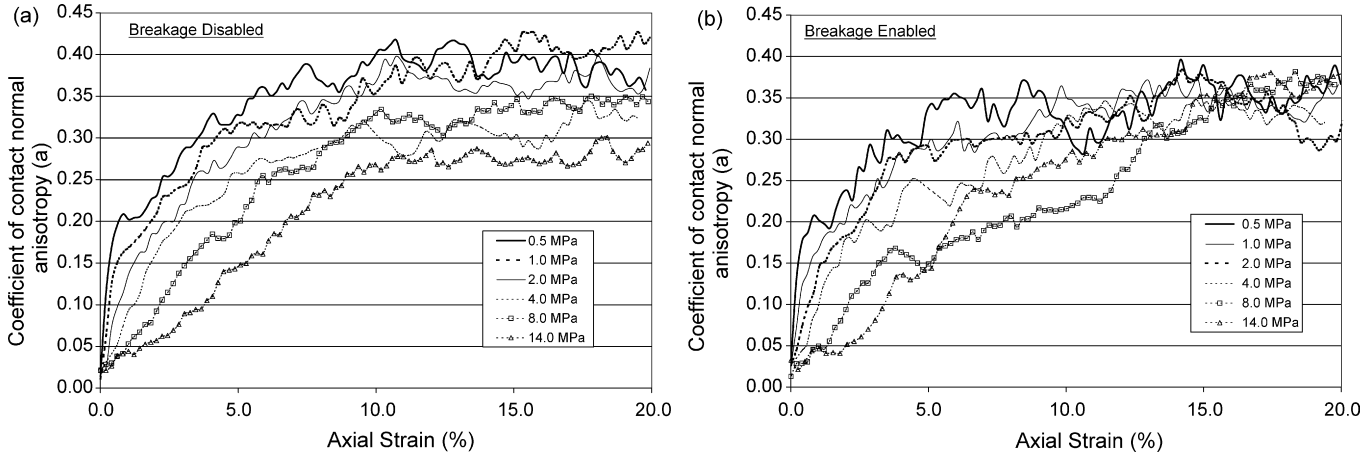

Fig. 16. Evolution of contact normal anisotropy coefficient: (a) NB tests; (b) WB tests.

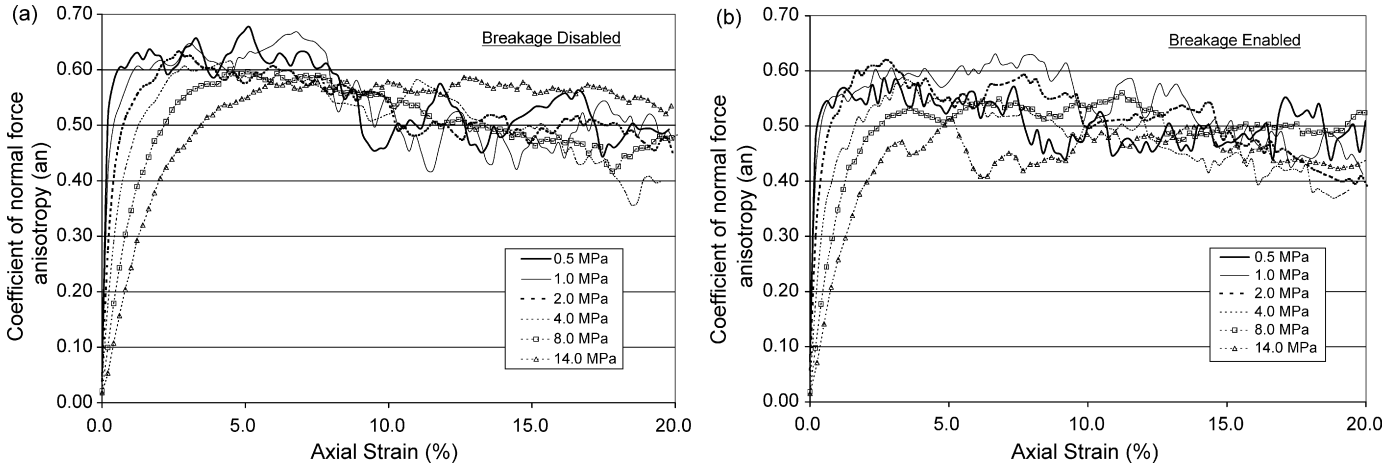

Fig. 17. Evolution of normal force anisotropy coefficient: (a) NB tests; (b) WB tests.

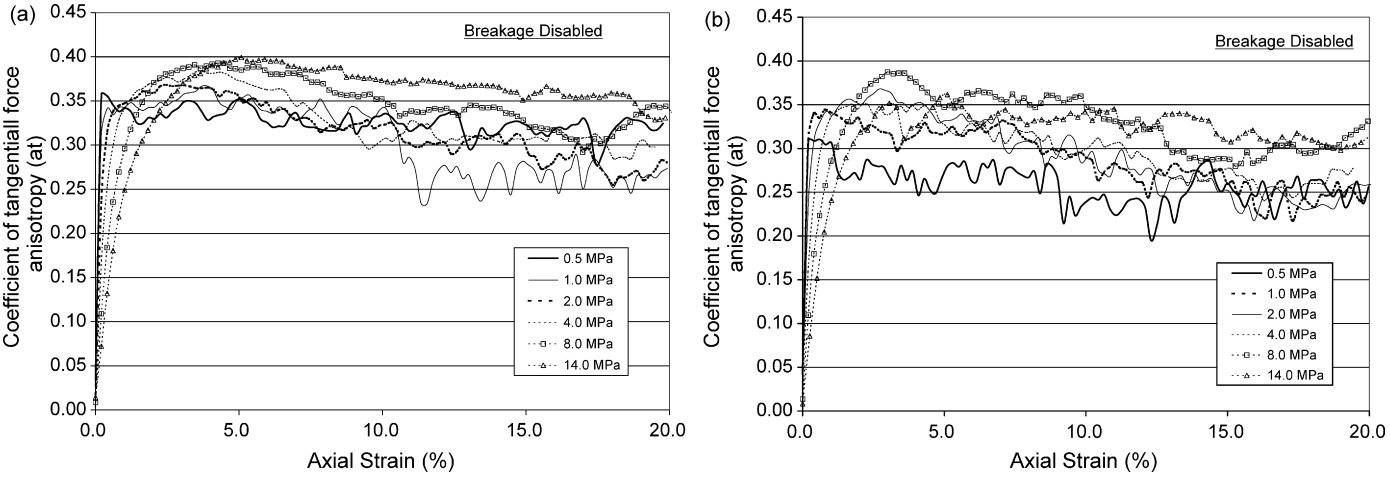

Fig. 18. Evolution of contact tangential force anisotropy coefficient: (a) NB tests; (b) WB tests.

Figs. 17 and 18 show the effect of stress level on the anisotropy coefficients of normal (a_n) and tangential forces (a_t), respectively. For both test series, the confining has a reverse effect on a_n and a_t parameters at low strain levels, but the trend is not clear with increasing axial strain. Generally, it can be observed that assemblies with lower confining pressure can provide more anisotropy in the media with subsequent higher shear strength. The higher the assembly is confined, the particles cannot move much freely and the particles shall tolerate their imposed forces in their obliged direction. So the anisotropy decreases both for normal and tangential parameters.

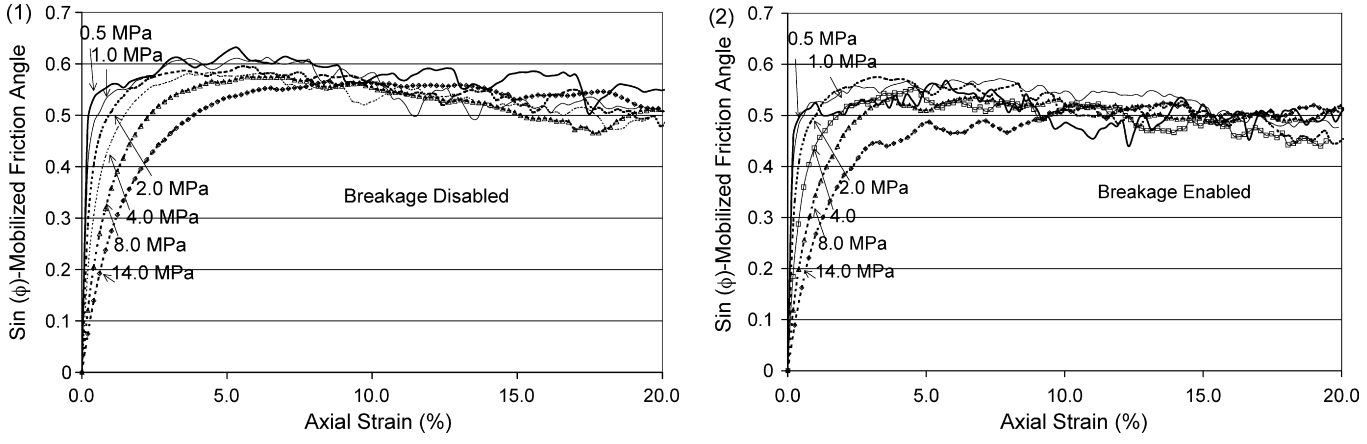

Fig. 19. Macromobilized friction angles versus axial strain for both groups of simulations.

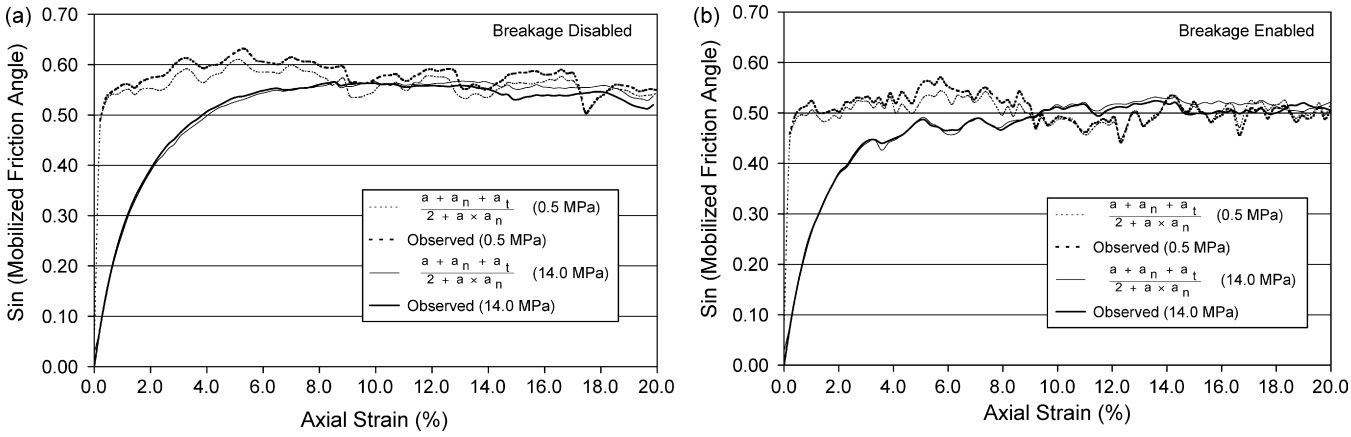

Fig. 20. Verification of stress–fabric relationship for assembly without breakable particles (a) and with breakable particles (b) at low and high stress levels.

4.4. Stress–fabric relationship

In a biaxial test, the mobilized internal friction angle of a cohesionless material can be determined by Eq. (12) as a function of major principal stresses:

$$\sin\,\phi = \frac{\sigma_2 - \sigma_1}{\sigma_2 + \sigma_1} = \frac{\sigma_2/\sigma_1 - 1}{\sigma_2/\sigma_1 + 1} \tag{12}$$

Major principal stresses are determined on the basis of the average stress tensor within an assembly. The stress tensor of an assembly with area of A could be calculated from the existing contact force f_i^C and contact vector l_j^C, as suggested by Rothenburg (1980):

$$\sigma_{ij} = \frac{1}{A}\sum_{C\in A} f_i^C l_j^C, \quad i, j = 1, 2 \tag{13}$$

The mobilized friction angle of the assemblies for both NB and WB tests are presented in Fig. 19 in the form of curves of $\sin\phi$ versus axial strain at different confining pressures. An increase of confining stress decreases the internal friction angle

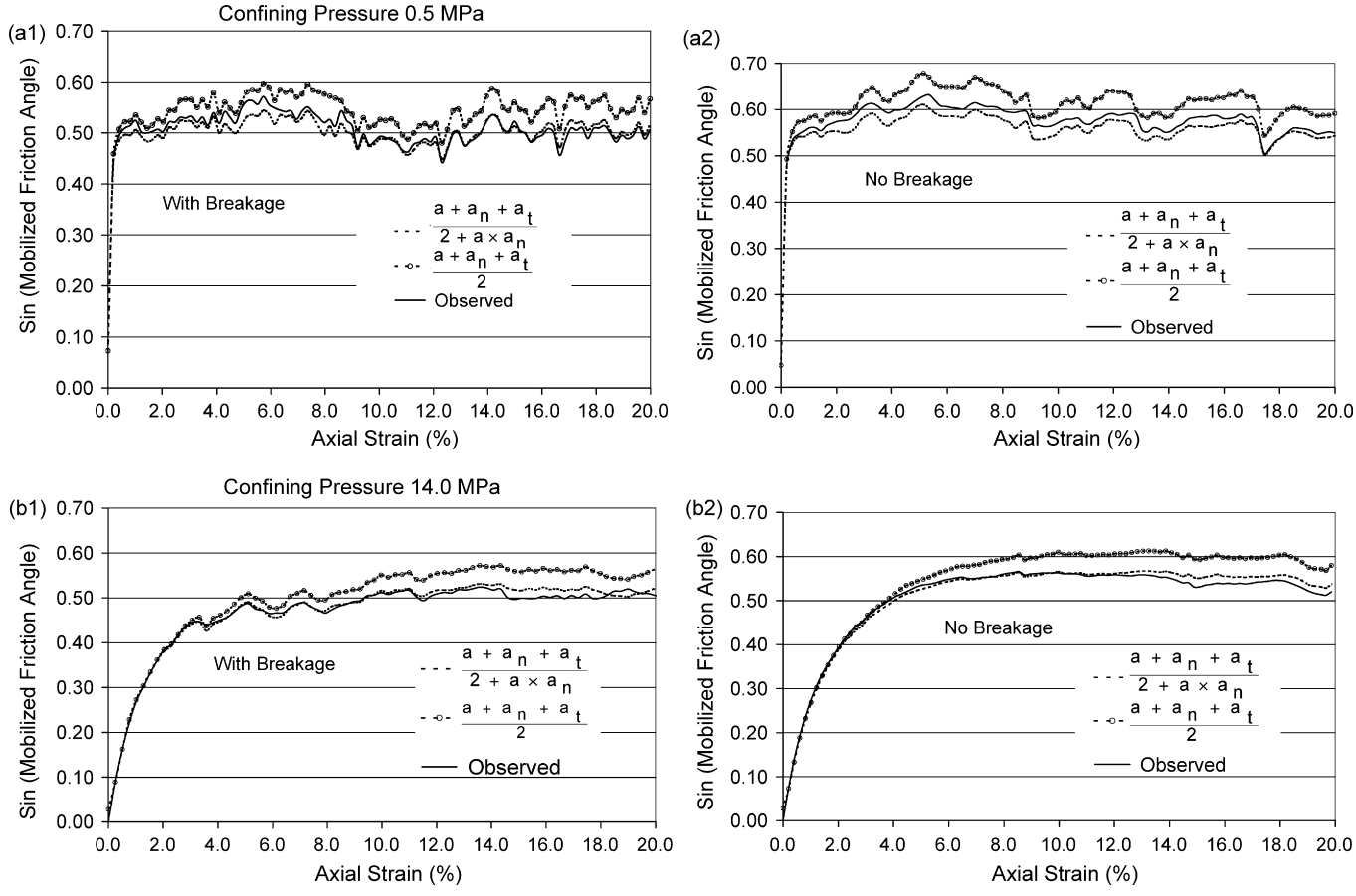

Fig. 21. Investigation on accuracy of stress–fabric relationships for sharp-edge particles at low stress level (a) and high confining status (b).

($\sin\phi$) and the sample fails at a higher axial stress. These effects are more intensive at higher stress levels. Comparison between the maximum mobilized friction angles of the tests reveals that particle breakage reduces the internal friction of rockfill materials at all stress levels.

Rothenburg and Bathurst (1989, 1992) derived a relationship between the measure of shear stress and the anisotropy coefficients of contact orientations and contact forces as follows:

$$\left(\frac{\sigma_2-\sigma_1}{\sigma_2+\sigma_1}\right)=\left(\frac{a+a_n+a_t}{2+a\times a_n}\right) \tag{14}$$

This expression suggests that the capacity of a granular assembly is directly attributable to its ability to develop anisotropy in contact orientations or to withstand directional variations of average contact forces. Fig. 20 compares the value of mobilized internal friction angle which is computed by the right-hand side of Eq. (14) and the other side of this equation in terms of macromechanics. As a result, the fabric expression is in agreement with the measured mobilized friction angle. The agreement is not affected by particle breakage and by stress level. So, it can be concluded that Eq. (14) could be employed to determine the friction angle of assemblies with breakable particles as well.

Rothenburg and Bathurst (1989) suggested a simplified expression to determine the mobilized friction angle for granular assemblies:

$$\sin\ \phi=\frac{1}{2}(a+a_n+a_t) \tag{15}$$

Fig. 21 illustrates the accuracy of this expression for determining the friction angle of rockfills, and shows that the simplified expression deviates more from simulation results.

5. Summary and conclusions

A numerical model combining DEM and FEM has been developed to simulate the breakage phenomena for sharp-edge particles. Two series of 2-dimensional biaxial tests with breakable and non-breakable particles have been simulated, microstructures of the samples are investigated during the shearing process, and the evolution of anisotropy coefficients is discussed. The influence of confining pressure on the mechanical behavior of simulated assemblies is also studied. Following are the main findings.

- Microstructure of 2D circular shaped assemblies shows that the breakage of particles in the assembly's centre is minimal and most breakage takes place along the shear bonds.
- The coordination number decreases after initial increasing (for high confining pressures), but the decreasing rate is limited by growing particle breakage.
- The normal force anisotropy (a_n) is the highest among all anisotropy coefficients. After initially evolving to some peak value, the coefficient of normal force anisotropy reduces slowly to some lower ultimate values at large axial strains in tests for low confining pressures, while, it retains its peak value in tests for high confining pressures.
- The anisotropy of contact normal increases continuously with shearing process due to the dilation of assemblies.
- The anisotropy of tangential force (a_t) grows rapidly to some peak value at the beginning of biaxial test and reduces slowly thereafter.
- Particle breakage overly reduces the anisotropy of an assembly during a biaxial test which causes less mobilization of the shear strength.
- Confining has a reverse effect on all anisotropy coefficients clearly at low strain levels.
- The stress–force–fabric expression developed by Rothenburg and Bathurst (1992) was verified for both assemblies of angular breakable and non-breakable particles.

Generally, assessment of the results indicates that particle breakage reduces internal friction but increases compressibility of the sample. Effect of the confining pressure on breakage is also considerable: higher confining pressures lead to a decrease in mobilized friction angle and an increase in materials compressibility.

References

Cheng, Y. P., Nakata, Y., & Bolton, M. D. (2003). Discrete element simulation of crushable soil. *Géotechnique*, *53*(7), 633–641.

Cundall, P. A. (1978). *Ball—A computer program to model granular media using distinct element method*. Technical Note TN-LN-13, Advanced Technology Group, Dams and Moore, London.

Cundall, P. A., & Hart, R. D. (1985). *Development of generalized 2-D and 3-D distinct element programs for modeling jointed rock*. Itasca Consulting Group, Misc. U.S. Army Corps of Engineers, Paper SL-85-1.

Edelbro, C. (2004). *Evaluation of rock mass strength criteria*. Doctoral dissertation, Luleå University of Technology, ISSN-I402-I757.

Ghabousi, J. (1997). Fully deformable discrete element analysis using a finite element approach. *International Journal of Computers and Geotechnics*, *5*, 175–195.

Hardin, B. O. (1985). Crushing of soil particles. *Journal of Geotechnical Engineering*, *111*(10), 1117–1192.

Hoek, E., & Brown, E. T. (1980). *Underground excavations in rock*. London: The Institution of Mining and Metallurgy.

Hoek, E., & Brown, E. T. (1997). Practical estimates of rock mass strength. *International Journal of Rock Mechanics and Mining Sciences and Geomechanics Abstracts*, *34*(8), 1165–1186.

Indraratna, B., Wijewardena, L. S. S., & Balasubramaniam, A. S. (1993). Large-scale triaxial testing of greywacke rock fill. *Géotechnique*, *43*(1), 37–51.

Itasca Consulting Group, Inc. (1999). *PFC3D (Particle Flow Code in Three Dimensions) Version 2. 00*. Minneapolis: ICG.

Kun, F., & Herrmann, H. J. (1996). A study of fragmentation process using a discrete element method. *Computer Methods in Applied Mechanics and Engineering*, *138*, 3–18.

Lade, P. V., & Yamamuro, J. A. (1996). Undrained sand behavior in axisymmetric tests at high pressures. *Journal of Geotechnical Engineering*, *122*(2), 120–129.

Lade, P. V., Yamamuro, J. A., & Bopp, P. A. (1996). Significance of particle crushing in granular materials. *Journal of Geotechnical Engineering*, *122*(4), 309–316.

Marinos, P., & Hoek, E. (2001). Estimating the geotechnical properties of heterogeneous rock masses such as flysch. *Bulletin of the Engineering Geology and the Environment*, *60*, 85–92.

Marsal, R. J. (1967). Large scale testing of rockfill materials. *Journal of the Soil Mechanics and Foundations Division, Proceedings of the American Society of Civil Engineers, 93*(SM2), 27–43.

Marsal, R. J. (1973). Mechanical properties of rockfill. In R. C. Hirshfeld & S. J. Poulos (Eds.), *Embankment-dam engineering, casagrande volume* (pp. 109–200). New York: John Wiley & Sons, Inc.

McDowell, G. R., & Harireche, O. (2002). Discrete element modelling of soil particle fracture. *Géotechnique*, *52*(2), 131–135.

Mirghasemi, A. A., Rothenburg, L., & Matyas, E. L. (1997). Numerical simulations of assemblies of two-dimensional polygon-shaped particles and effects of confining pressure on shear strength. *Soils and Foundations*, *37*(3), 43–52.

Mirghasemi, A. A., Rothenburg, L., & Matyas, E. L. (2002). Influence of particle shape on engineering properties of assemblies of two dimensional polygon-shaped particles. *Géotechnique*, *52*(3), 209–217.

Mohammadi, S., Owen, D. R. J., & Peric, D. (1998). A combined finite/discrete element algorithm for delamination analysis of composites. *Finite Elements in Analysis and Design*, *28*, 321–336.

Potapov, A. V., & Campbell, C. S. (1994). Computer simulation of impact-induced particle breakage. *Powder Technology*, *81*, 207–216.

Potapov, A. V., & Campbell, C. S. (1997). Computer simulation of shear-induced particle attrition. *Powder Technology*, *94*, 109–122.

Robertson, D., & Bolton, M. D. (2001). DEM simulations of crushable grains and soils. In *Proceedings of the Powder and Grains, Sendai* (pp. 623–626).

Rothenburg, L. (1980). *Micromechanics of idealized granular systems* (p. 332). Doctoral dissertation, Department of Civil Engineering, Carleton University, Ottawa, Ontario.

Rothenburg, L., & Bathurst, R. J. (1989). Analytical study of induced anisotropy in idealized granular materials. *Géotechnique*, *39*(4), 601–614.

Rothenburg, L., & Bathurst, R. J. (1992). Micromechanical features of granular assemblies with planar elliptical particles. *Géotechnique*, *42*(1), 79–95.

Rothenburg, L., Bathurst, R. J., & Dusseault, M. B. (1989). Micromechanical ideas in constitutive modeling of granular materials. In: J. Biarez & R. Gourvès (Eds.), *Powders and Grains*. Rotterdam: Balkema. ISBN: 906191 984 3.

Seyedi Hosseininia, E., & Mirghasemi, A. A. (2006). Numerical simulation of breakage of two-dimensional polygon-shaped particles using discrete element method. *Powder Technology*, *166*, 100–112.

Seyedi Hosseininia, E., & Mirghasemi, A. A. (2007). Effect of particle breakage on the behavior of simulated angular particle assemblies. *China Particuology*, *5*, 328–336.

Thornton, C., & Barnes, D. J. (1986). Computer simulated deformation of compact granular assemblies. *Acta Mechanica*, *64*, 45–61.

Varadarajan, A., Sharma, K. G., Venkatachalam, K., & Gupta, A. K. (2003). Testing and modelling two rockfill materials. *Journal of Geotechnical and Geoenvironmental Engineering, ASCE*, *129*(3), 206–218.

Yamamuro, J. A., & Lade, P. V. (1996). Drained sand behavior in axisymmetric tests at high pressures. *Journal of Geotechnical Engineering*, *122*(2), 109–119.